sensors

MDPI

Article

Preparation of $Eu_{0.075}Tb_{0.925}$-Metal Organic Framework as a Fluorescent Probe and Application in the Detection of Fe^{3+} and $Cr_2O_7^{2-}$

Jie Yin, Hongtao Chu *, Shili Qin, Haiyan Qi and Minggang Hu

College of Chemistry and Chemical Engineering, Qiqihaer University, Qiqihaer 161006, China; yinjie199707@163.com (J.Y.); qinshili1103@163.com (S.Q.); lange19791@163.com (H.Q.); hmgxs@163.com (M.H.)
* Correspondence: lange19790@163.com; Tel.: +86-13504525400

Abstract: Luminescent Ln-MOFs ($Eu_{0.075}Tb_{0.925}$-MOF) were successfully synthesised through the solvothermal reaction of $Tb(NO_3)_3{\cdot}6H_2O$, $Eu(NO_3)_3{\cdot}6H_2O$, and the ligand pyromellitic acid. The product was characterised by X-ray diffraction (XRD), TG analysis, EM, X-ray photoelectron spectroscopy (XPS), and luminescence properties, and results show that the synthesised material $Eu_{0.075}Tb_{0.925}$-MOF has a selective ratio-based fluorescence response to Fe^{3+} or $Cr_2O_7^{2-}$. On the basis of the internal filtering effect, the fluorescence detection experiment shows that as the concentration of Fe^{3+} or $Cr_2O_7^{2-}$ increases, the intensity of the characteristic emission peak at 544 nm of Tb^{3+} decreases, and the intensity of the characteristic emission peak at 653 nm of Eu^{3+} increases in $Eu_{0.075}Tb_{0.925}$-MOF. The fluorescence intensity ratio (I_{653}/I_{544}) has a good linear relationship with the target concentration. The detection linear range for Fe^{3+} or $Cr_2O_7^{2-}$ is 10–100 μM/L, and the detection limits are 2.71×10^{-7} and 8.72×10^{-7} M, respectively. Compared with the sensor material with a single fluorescence emission, the synthesised material has a higher anti-interference ability. The synthesised $Eu_{0.075}Tb_{0.925}$-MOF can be used as a highly selective and recyclable sensing material for Fe^{3+} or $Cr_2O_7^{2-}$. This material should be an excellent candidate for multifunctional sensors.

Keywords: Ln-MOFs; luminous sensing; Fe^{3+}; $Cr_2O_7^{2-}$

Citation: Yin, J.; Chu, H.; Qin, S.; Qi, H.; Hu, M. Preparation of $Eu_{0.075}Tb_{0.925}$-Metal Organic Framework as a Fluorescent Probe and Application in the Detection of Fe^{3+} and $Cr_2O_7^{2-}$. *Sensors* **2021**, *21*, 7355. https://doi.org/10.3390/s21217355

Academic Editor: Claudio Pellecchia

Received: 29 September 2021
Accepted: 3 November 2021
Published: 5 November 2021

1. Introduction

Heavy metals and inorganic anion pollutants in water pose hidden dangers to human health [1]. The United Nations Sustainable Development Goals set in September 2015 indicated that countries are expected to greatly improve human water quality by 2030. Thus, the detection of pollutants in water has become increasingly important. Fe^{3+} is one of the basic trace elements in humans. The lack or excess of this element can cause many physiological disorders, such as nausea, abdominal pain, anaemia, liver cirrhosis, and organ failure [2–4]. Salonen et al. [2] confirmed that elevated iron content is an important risk factor for acute myocardial infarction, Bijeh et al. [3] confirmed that the increased risk of cardiovascular disease is related to elevated iron content, and Jehn et al. [4] confirmed that elevated iron could lead to abnormal baseline metabolism. In addition, $Cr_2O_7^{2-}$ is an important oxidant in laboratories and industry [5], and it is highly carcinogenic in the environment and harmful to the ecology, environment, and biological system [6–9]. Mansi et al. [6] confirmed that it is the second most abundant inorganic groundwater pollutant due to its wide application in many industrial fields, such as electroplating chrome, dyes, and leather tanning. Costa [7] confirmed that it is mutagenic and carcinogenic to organisms' sexual function. Therefore, the selective sensing of Fe^{3+} and $Cr_2O_7^{2-}$ in water quality has attracted growing attention from scholars. Many methods are used for the determination of Fe^{3+} and $Cr_2O_7^{2-}$, such as atomic emission spectrometry, atomic absorption spectrometry, inductively coupled plasma mass spectrometry, electrochemical methods, and ion chromatography. However, these methods are complicated to operate,

costly, and have a long detection time. Therefore, developing a simple and efficient method to determine Fe^{3+} and $Cr_2O_7^{2-}$ is of practical significance. Fluorescence sensing technology can meet the requirements of new analysis and detection technology due to its high sensitivity, fast analysis speed, strong selectivity, simple operation, and low experimental cost. In recent years, it has received extensive attention [10].

Ln-MOFs materials refer to the self-assembly connection of metal ions and organic ligands by coordination bonds to form network complexes. Ln-MOFs materials have outstanding luminescence characteristics; that is, they have the advantages of large Stokes shift, high quantum yield and luminescence intensity, narrow emission spectrum range, flexible coordination mode, and long luminescence life. MOFs fluorescent probes are commonly used as sensors [11–27]. Hna et al. [26] synthesised Ce-MOF to detect Fe^{3+}, and Gai et al. [27] synthesised dual-sensor Eu-MOF to detect Fe^{3+} and $Cr_2O_7^{2-}$. The ratio fluorescent probe is based on measuring the ratio of the fluorescence intensity of two independent fluorescence emission peaks for quantitative analysis, which can effectively reduce the influence of excitation light, environment, and probe concentration changes, and greatly improve the accuracy of the method. At present, the usual design method of the Ln-MOFs ratio probe is to select two kinds of Ln^{3+} to synthesise by different molar ratios [28–30] or to combine Ln-MOFs with one or two substances with different fluorescence emission wavelengths, including carbon dots (CDs), quantum dots, and fluorescent dyes [31–35]. Zhang et al. [30] used two different molar ratios of Tb and Eu as the metal centre. 2,2′-bipyridine-6,6′-dicarboxylate acid (H_2bpdc) is a ligand to synthesise $Eu_{0.6059}Tb_{0.3941}$-ZMOF, which can realise the selective detection of haemolysed phosphate (lysophosphatidic acid or LPA) in human plasma. Xu et al. [31] reported that CDs with strong fluorescence activity and Eu^{3+} were encapsulated in MOF-253, and the dual-emission ratio probe Eu^{3+}/CDs@MOF-253 was synthesised to detect Hg^{2+}. Therefore, the development of ratio fluorescent probe Ln-MOFs to detect Fe^{3+} and $Cr_2O_7^{2-}$ has great application prospects.

The selective fluorescence detection of Fe^{3+} and $Cr_2O_7^{2-}$ using ratio fluorescent probe Ln-MOFs is rarely reported in the literature. In this paper, luminescent $Eu_{0.075}Tb_{0.925}$-MOF was successfully synthesised by the solvothermal reaction of $Tb(NO_3)_3{\cdot}6H_2O$, $Eu(NO_3)_3{\cdot}6H_2O$, and ligand pyromellitic acid. $Eu_{0.075}Tb_{0.925}$-MOF was comprehensively characterised by XRD, thermogravimetric analysis (TG), elemental analysis, Fourier transform infrared spectroscopy (FTIR), transmission electron microscope (TEM), scanning electron microscope (SEM), and XPS. $Eu_{0.075}Tb_{0.925}$-MOF has excellent stability in aqueous solution, and it can detect Fe^{3+} and $Cr_2O_7^{2-}$ in aqueous solution by dual-emission ratio fluorescence sensing, which provides a new idea for the fluorescence detection of Fe^{3+} and $Cr_2O_7^{2-}$.

2. Materials and Methods

Commercially available reagents and solvents were used. XRD characterisation was performed to determine the regular arrangement of atoms or ions in the $Eu_{0.075}Tb_{0.925}$-MOF, which is one of the commonly used methods to explore the structure of matter. An elemental analyser was used for elemental analysis. FTIR was used to scan and analyse the range of 4000–400 cm^{-1} to determine the functional groups and chemical bonds of $Eu_{0.075}Tb_{0.925}$-MOF. The thermal stability of $Eu_{0.075}Tb_{0.925}$-MOF was analysed by TG, which was performed under N_2 protection. TEM and SEM were used to observe the specific morphology of $Eu_{0.075}Tb_{0.925}$-MOF. The FL/FS900 fluorescence spectrometer was used to record the steady-state luminescence performance of $Eu_{0.075}Tb_{0.925}$-MOF. XPS and UV spectrophotometers were used to investigate the reaction mechanism.

Synthesis of $Eu_{0.075}Tb_{0.925}$-MOF: Product preparation was the first step. $Eu_{0.075}Tb_{0.925}$-MOF with Tb and Eu were prepared as the metal centre, and pyromellitic acid was prepared as the organic ligand as follows: Dissolved $Tb(NO_3)_3{\cdot}6H_2O$ + $Eu(NO_3)_3{\cdot}6H_2O$ (0.2 mmol), pyromellitic acid (0.2 mmol), DMF (8 mL), distilled water (4 mL), and CH_3CH_2OH (4 mL) were transferred to an autoclave (volume: 25 mL). The product was then sealed and heated in a 120 °C vacuum drying oven for 48 h and gradually cooled to ambient temperature. After the autoclave was opened, the product was collected after centrifugation, washed

thoroughly with DMF and ethanol, paralleled three times, and dried. Thus, the target product $Eu_{0.075}Tb_{0.925}$-MOF was obtained.

3. Results and Discussion

3.1. XRD Characterisation

Eu-MOF, Tb-MOF, and $Eu_{0.075}Tb_{0.925}$-MOF combined with lanthanide nitrate and pyromellitic acid were prepared by the solvothermal method. Figure 1 shows the XRD patterns of Ln-MOFs. As shown in the figure, the 2θ diffraction angle peak positions of the simulated XRD pattern and the synthesised samples Eu-MOF, Tb-MOF, and $Eu_{0.075}Tb_{0.925}$-MOF are the same, and there are sharp peaks at the diffraction angles from 9 to 10. At the same time, the diffraction peaks 9 to 10 of the crystal synthesised by Silva et al. [36] are basically the same, indicating that the synthesised $Eu_{0.075}Tb_{0.925}$-MOF has high purity and good crystallinity [36–39].

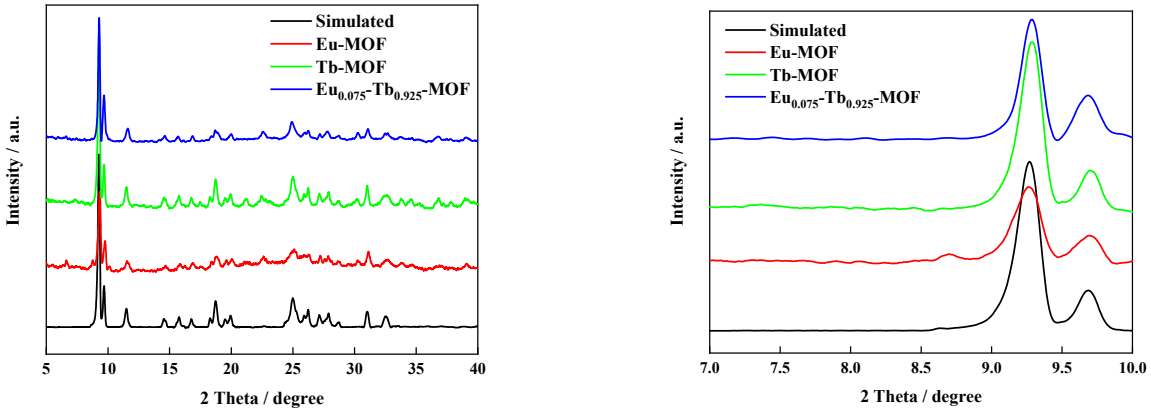

Figure 1. (**a**) XRD patterns of Ln-MOFs. (**b**) Enlarged version.

3.2. TG Analysis

Figure 2 shows the TG analysis results of Ln-MOFs. The weight loss of Ln-MOFs is mainly divided into two stages. Before 340 °C, $Eu_{0.075}Tb_{0.925}$-MOF has good thermal stability.

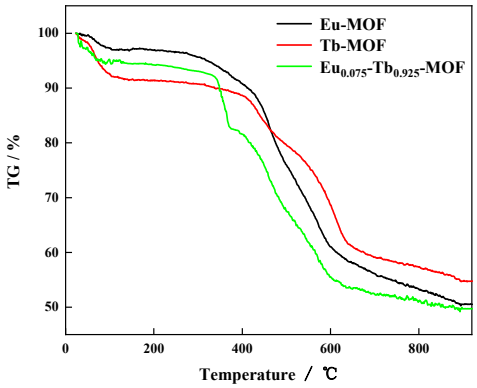

Figure 2. TG of Ln-MOFs.

3.3. FTIR Analysis

Figure 3 shows the FTIR spectrum of Ln-MOFs. Compared with the FTIR spectrum of pyromellitic acid, the main characteristic peaks in the FTIR spectrum of $Eu_{0.075}Tb_{0.925}$-MOF are similar to those of pyromellitic acid, but the C=O stretching vibration peak disappeared at 1720 cm^{-1} in the original pyromellitic acid spectrum (significantly weakened), thereby indicating that the carboxyl oxygen is coordinated with Tb and Eu atoms in the ligand.

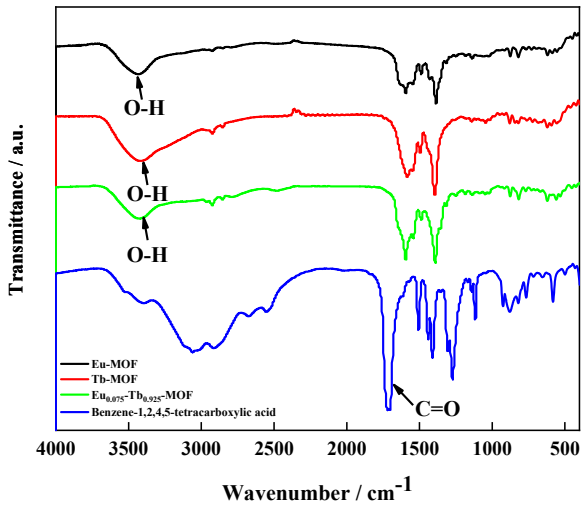

Figure 3. FTIR spectra of Benzene-1,2,4,5-tetracarboxylic acid and Ln-MOFs.

3.4. Elemental Analysis and XPS

A comparison of elemental (Table 1) and XPS (Figure 4) analyses shows that, corresponding to the content of the element, the distribution ratio of Eu to Tb in $Eu_{0.075}Tb_{0.925}$-MOF is 0.075:0.925. The specific loadings of $Tb(NO_3)_3$ and $Eu(NO_3)_3$ are 42.74% and 3.46% respectively, and the cooling rate is 0.017 K/s.

Table 1. Element analysis table.

Ln-MOFs	C	H	N	O	Eu/Tb
Eu-MOF	30.37%	1.87%	1.87%	26.64%	39.25%
Tb-MOF	22.01%	1.84%	1.13%	26.11%	48.91%
$Eu_{0.075}Tb_{0.925}$-MOF	23.53%	1.85%	1.56%	26.85%	46.21%

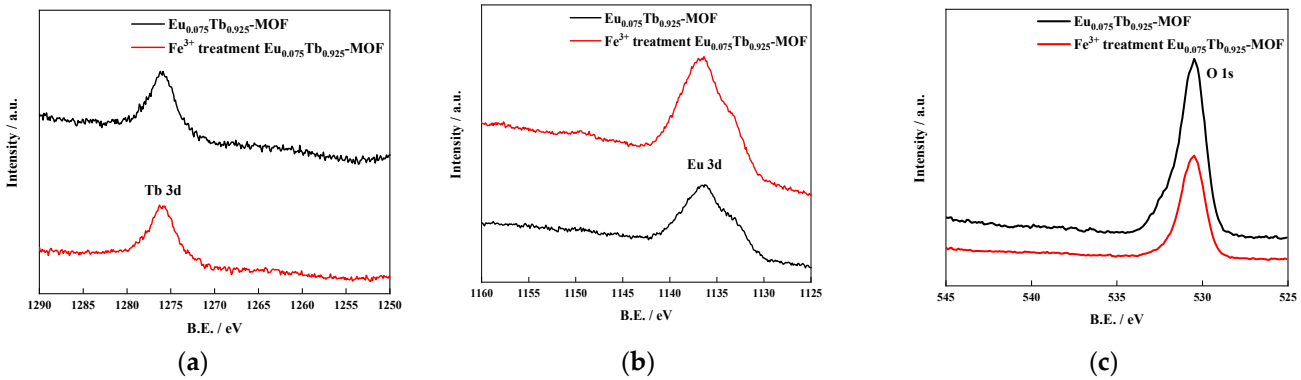

Figure 4. XPS of $Eu_{0.075}Tb_{0.925}$-MOF before and after Fe^{3+} addition: (**a**) Tb 3d, (**b**) Eu 3d, and (**c**) O 1s.

3.5. EM Characterisation

Figure 5 shows the TEM and SEM images of $Eu_{0.075}Tb_{0.925}$-MOF, which indicate that the prepared $Eu_{0.075}Tb_{0.925}$-MOF has a regular external morphology, a nanocolumn shape, and a diameter of about 500 nm.

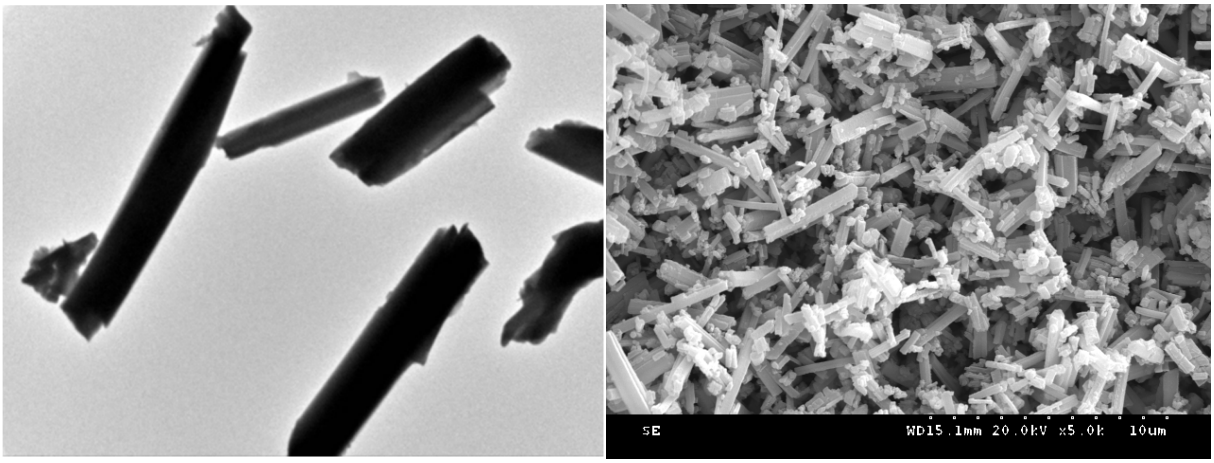

(**a**) (**b**)

Figure 5. (**a**) TEM and (**b**) SEM of $Eu_{0.075}Tb_{0.925}$-MOF.

3.6. Adsorption Characteristics of $Eu_{0.075}Tb_{0.925}$-MOF

Figure 6 shows the N_2 adsorption desorption isotherms of $Eu_{0.075}Tb_{0.925}$-MOF. The adsorption capacity increases slowly with the increase of pressure at the middle–high-pressure stage, indicating that $Eu_{0.075}Tb_{0.925}$-MOF is a porous material with an average pore size of 3.38 nm, a BJH average pore diameter of 20.99 nm, and a BET specific surface area of 12.9542 m^2/g.

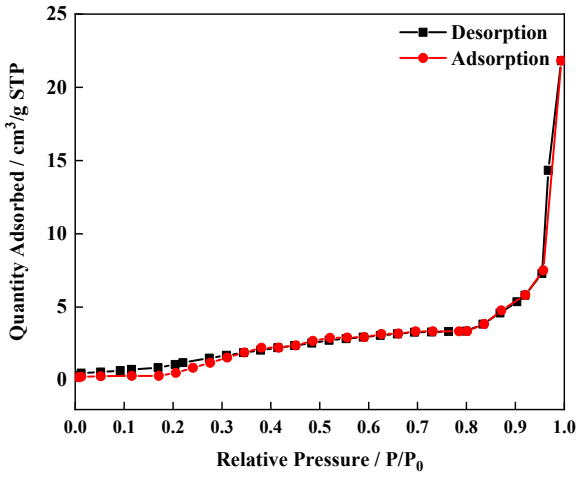

Figure 6. The N_2 adsorption desorption isotherms of $Eu_{0.075}Tb_{0.925}$-MOF.

3.7. Photoluminescence Characteristics

Figure 7a shows the fluorescence emission spectrum of $Eu_{0.075}Tb_{0.925}$-MOF measured at ambient temperature. The figure shows that $Eu_{0.075}Tb_{0.925}$-MOF exhibits characteristic transitions of Tb^{3+} and Eu^{3+} under the excitation of 310 nm light, located at 544 and 653 nm respectively, showing the same intensity of fluorescence emission. This finding indicates that the ligand can effectively transfer energy to Tb^{3+} and Eu^{3+} at the same time [40–44].

As shown in the CIE diagram in Figure 7c,d, Eu-MOF shows red fluorescence, and Tb-MOF shows green fluorescence. When Eu^{3+} and Tb^{3+} synthesise $Eu_{0.075}Tb_{0.925}$-MOF at a ratio of 0.075:0.925, $Eu_{0.075}Tb_{0.925}$-MOF shows the intermediate colour of the two, which is a yellow-green fluorescence sensitive to the human eye. This material has potential application as a luminescent material and a light-sensitive material for naked-eye detection [45].

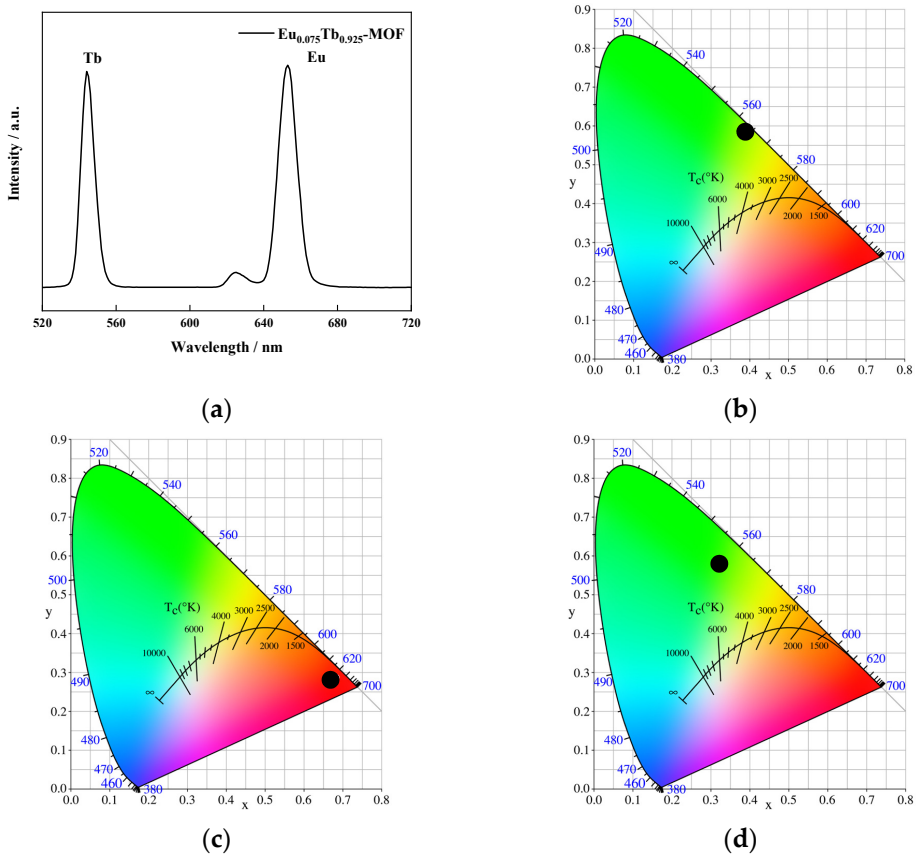

Figure 7. (**a**) Emission spectra of $Eu_{0.075}Tb_{0.925}$-MOF, (**b**) CIE of $Eu_{0.075}Tb_{0.925}$-MOF, (**c**) CIE of Eu-MOF, and (**d**) CIE of Tb-MOF.

3.8. Fluorescence Sensing of Fe^{3+}

Gao and Ma [46,47] prepared Tb-MOF and used it for sensitive fluorescence sensing of Fe^{3+} and $Cr_2O_7^{2-}$. On this basis, this paper designs a ratio fluorescent probe, $Eu_{0.075}Tb_{0.925}$-MOF, for the fluorescence sensing of Fe^{3+} and $Cr_2O_7^{2-}$ to improve the measurement accuracy and expand the linear range of the test. To determine the fluorescence performance of $Eu_{0.075}Tb_{0.925}$-MOF to Fe^{3+}, the fluorescence response of $Eu_{0.075}Tb_{0.925}$-MOF to Fe^{3+} was investigated, and the results are shown in Figure 8.

Figure 8a shows that with the increase of the Fe^{3+} concentration, the characteristic emission peak intensity of Tb^{3+} decreases at 544 nm, and the characteristic emission peak intensity of Eu^{3+} increases at 653 nm. The intensity at I_{Eu} = 653 nm and I_{Tb} = 544 nm is used to calculate the intensity change I_0/I, where I_0 (I_{Eu0}/I_{Tb0}) is the initial fluorescence intensity before fluorescence, and I (I_{Eu}/I_{Tb}) is the fluorescence intensity in the presence of Fe^{3+}. Figure 8b shows that I_0/I and Fe^{3+} present a linear relationship in the concentration range of 10–100 μM/L, and the linear regression equation is:

$$I_0/I = 0.71 - 7948.64x. \quad (1)$$

The limit of detection (LOD) of Fe^{3+} is evaluated by the equation $3S_b/S$, where S_b is the standard deviation of repeated detection of the original solution, and S is the slope of the linear fit. The LOD is calculated as 2.71×10^{-7} M. Figure 8c shows that the colour change trend of $Eu_{0.075}Tb_{0.925}$-MOF is yellow green–yellow–orange–red with the increase in Fe^{3+} concentration. This material is expected to achieve naked-eye detection of Fe^{3+}.

The prepared $Eu_{0.075}Tb_{0.925}$-MOF was subjected to a cyclic application experiment, and KNO_3 solution was used to wash the used materials. Figure 8d,e shows that the ratio of the luminous intensity of the material and the XRD did not change considerably, even after five cycles. $Eu_{0.075}Tb_{0.925}$-MOF is very stable in the sensing experiment.

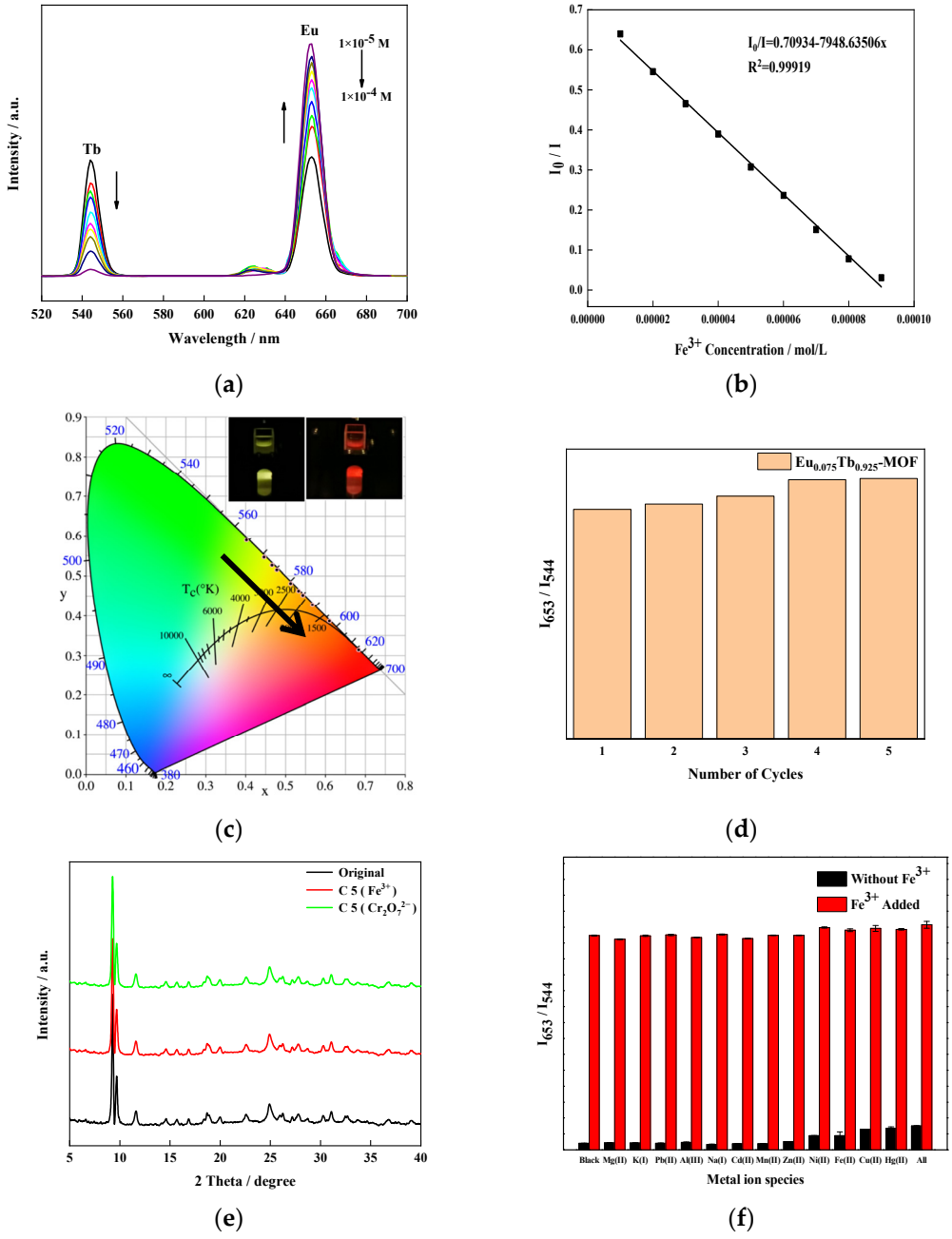

Figure 8. (**a**) The emission spectra of $Eu_{0.075}Tb_{0.925}$-MOF dispersions with different Fe^{3+} concentrations under 310 nm excitation light. (**b**) Calibration line with Fe^{3+}(in the range of 10–100 μM/L), (**c**) CIE, (**d**) cycles of $Eu_{0.075}Tb_{0.925}$-MOF, (**e**) XRD pattern of $Eu_{0.075}Tb_{0.925}$-MOF after five cycles, and (**f**) I_{Eu}/I_{Tb} histogram of $Eu_{0.075}Tb_{0.925}$-MOF dispersion containing metallic cations.

The fluorescence sensing selectivity of $Eu_{0.075}Tb_{0.925}$-MOF to Fe^{3+} was investigated through the anti-interference experiment. The $Eu_{0.075}Tb_{0.925}$-MOF sample was immersed in NaX solution (Mg^{2+}, K^+, Pb^{2+}, Al^{3+}, Na^+, Cd^{2+}, Mn^{2+}, Zn^{2+}, Ni^{2+}, Fe^{2+}, Cu^{2+}, Hg^{2+}) at a concentration of 1×10^{-4} M. The results are shown in Figure 8f. Except for Fe^{3+}, the luminous intensity ratio of $Eu_{0.075}Tb_{0.925}$-MOF exhibits almost no change after the addition of metal ions. However, when the same amount of Fe^{3+} was added to the Mg^{2+}, K^+, Pb^{2+}, Al^{3+}, Na^+, Cd^{2+}, Mn^{2+}, Zn^{2+}, Ni^{2+}, Fe^{2+}, Cu^{2+}, and Hg^{2+} solution containing $Eu_{0.075}Tb_{0.925}$-MOF, the luminous intensity ratio of I_{Eu}/I_{Tb} was significantly higher. This result shows that the sensing ability of $Eu_{0.075}Tb_{0.925}$-MOF on Fe^{3+} will not be interfered with by the

presence of other metal ions. Therefore, $Eu_{0.075}Tb_{0.925}$-MOF has a high selectivity for Fe^{3+} in an aqueous solution.

3.9. Fluorescence Sensing of $Cr_2O_7^{2-}$

To determine the fluorescence performance of $Eu_{0.075}Tb_{0.925}$-MOF to $Cr_2O_7^{2-}$, the fluorescence response of $Eu_{0.075}Tb_{0.925}$-MOF to $Cr_2O_7^{2-}$ was investigated, and the results are shown in Figure 9.

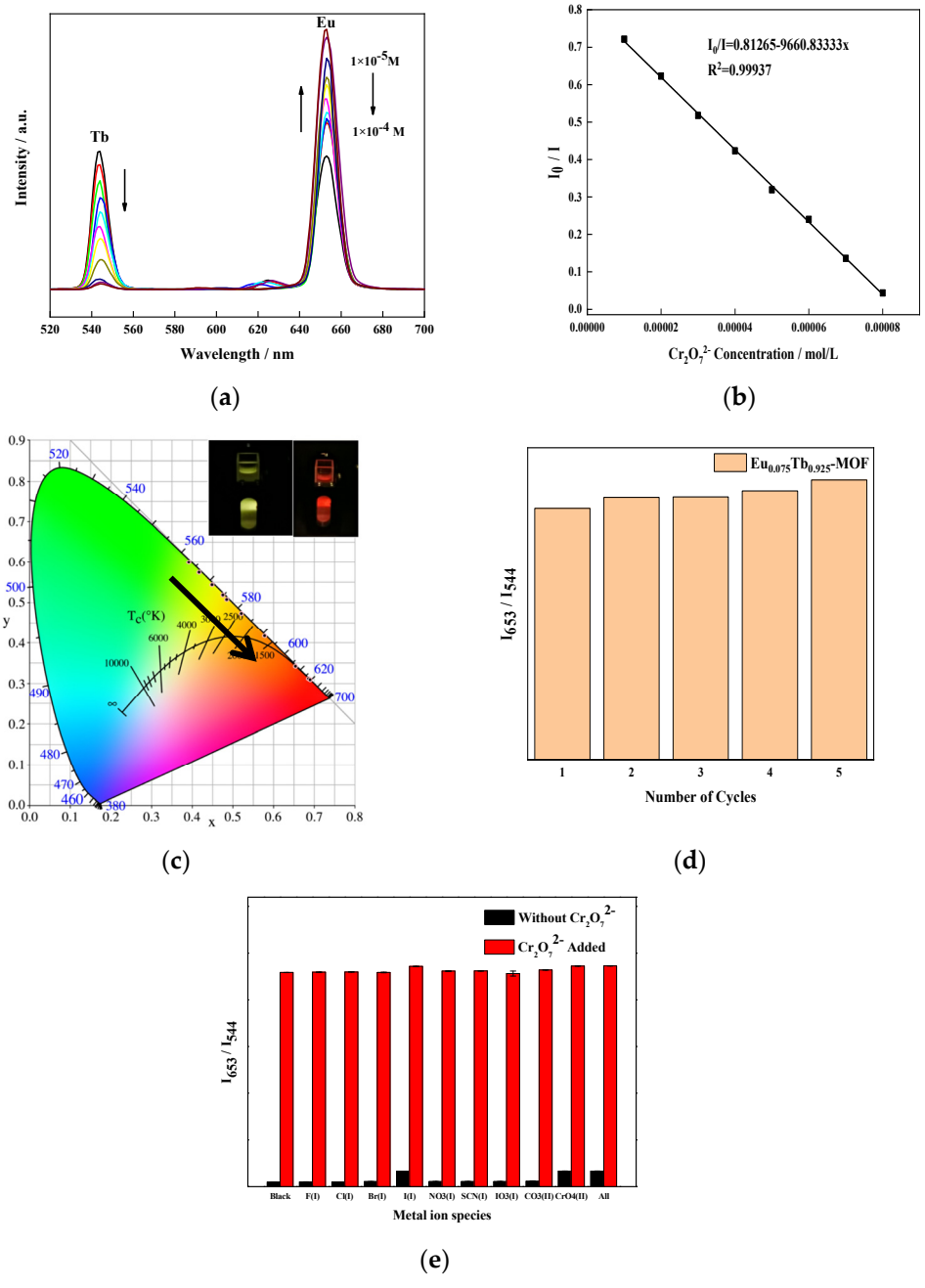

Figure 9. (**a**) The emission spectra of $Eu_{0.075}Tb_{0.925}$-MOF dispersions with different $Cr_2O_7^{2-}$ concentrations under 310 nm excitation light. (**b**) Calibration line with $Cr_2O_7^{2-}$(in the range of 10–100 μM/L), (**c**) CIE, (**d**) cycles of $Eu_{0.075}Tb_{0.925}$-MOF, and (**e**) I_{Eu}/I_{Tb} histogram of $Eu_{0.075}Tb_{0.925}$-MOF dispersion containing anions.

Figure 9a shows that with the increase in $Cr_2O_7^{2-}$ concentration, the characteristic emission peak intensity of Tb^{3+} decreases at 544 nm, and the characteristic emission peak

intensity of Eu^{3+} increases at 653 nm. At the same time, I_0/I and $Cr_2O_7^{2-}$ showed a linear correlation in the concentration range of 10–100 μM/L, the linear regression equation is:

$$I_0/I = 0.81 - 9660.83x, \quad (2)$$

and the LOD was 8.72×10^{-7} M. The CIE diagram in Figure 9c shows that with the increase in $Cr_2O_7^{2-}$ concentration, the colour change trend of $Eu_{0.075}Tb_{0.925}$-MOF is yellow green–yellow–orange–red, which is expected to realise the naked-eye detection of $Cr_2O_7^{2-}$.

A cyclic application experiment was performed on $Eu_{0.075}Tb_{0.925}$-MOF. Figure 9d shows that the luminous intensity ratio of $Eu_{0.075}Tb_{0.925}$-MOF does not change much after five cycles. $Eu_{0.075}Tb_{0.925}$-MOF was very stable in the sensing experiment.

Similarly, the fluorescence sensing selectivity of $Eu_{0.075}Tb_{0.925}$-MOF to $Cr_2O_7^{2-}$ was investigated through the anti-interference experiment. $Eu_{0.075}Tb_{0.925}$-MOF was dispersed into a solution containing F^-, Cl^-, I^-, Br^-, NO_3^-, CrO_4^{2-}, SCN^-, IO_3^-, CO_3^{2-}, and $Cr_2O_7^{2-}$ with the same concentration. The results are shown in Figure 9e. Except for $Cr_2O_7^{2-}$, the luminous intensity ratio of $Eu_{0.075}Tb_{0.925}$-MOF is almost unchanged after the addition of anions. However, when the same amount of $Cr_2O_7^{2-}$ was added to the F^-, Cl^-, I^-, Br^-, NO_3^-, CrO_4^{2-}, SCN^-, IO_3^-, and CO_3^{2-} solution containing $Eu_{0.075}Tb_{0.925}$-MOF, the luminous intensity ratio of I_{Eu}/I_{Tb} was significantly higher. This result shows that the sensing ability of $Eu_{0.075}Tb_{0.925}$-MOF on $Cr_2O_7^{2-}$ will not be interfered with by the presence of other anions. Therefore, $Eu_{0.075}Tb_{0.925}$-MOF has a high selectivity for $Cr_2O_7^{2-}$ in an aqueous solution.

3.10. Comparison with Other Sensors That Detect Fe^{3+} and $Cr_2O_7^{2-}$ Ions

Compared with the Fe^{3+} and $Cr_2O_7^{2-}$ detection methods used in other studies, as shown in Table 2, the prepared $Eu_{0.075}Tb_{0.925}$-MOF can reduce the effects of interference caused by excitation light, the environment, and probe concentration changes, and it has improved the detection accuracy relative to other methods.

Table 2. Comparison of the reported methods for Fe^{3+} and $Cr_2O_7^{2-}$ using Ln-MOFs.

Ln-MOFs	Detect Ion	LOD (M)	Ratio Fluorescent Probe	Linear Range	References
$Eu_{0.075}Tb_{0.925}$-MOF	Fe^{3+} $Cr_2O_7^{2-}$	2.71×10^{-7} 8.72×10^{-7}	Dual emission	10–100 μM (R^2 = 0.99919, R^2 = 0.99937)	This work
Eu-MOF; Tb-MOF [Eu/Tb, 4,4′-(((5-carboxy-1,3-phenylene)bis(azanediyl))bis(carbonyl)) dibenzoic acid]	Fe^{3+} $Cr_2O_7^{2-}$	1×10^{-5} 8.94×10^{-5}	Single emission	0–1.0 mM (R^2 = 0.9021, R^2 = 0.9752)	[47]
Eu-MOF [Eu, 5-(2′,5′-dicarboxylphenyl) picolinic acid ligand]	Fe^{3+} $Cr_2O_7^{2-}$	5.7×10^{-7} 4.2×10^{-7}	Single emission	0–50 μM (R^2 = 0.9948, R^2 = 0.9979)	[48]
Tb-MOF [Tb,H3BTB]	Fe^{3+}	1×10^{-5}	Single emission	-	[49]
Eu-MOF [Eu, 2-aminoterephthalic acid 1,10-phenanthroline]	Fe^{3+}	4.5×10^{-5}	Single emission	0–0.25 mM (R^2 = 0.992)	[50]
Tb-MOF [Tb, 2-(2-carboxyphenoxy)terephthalic acid]	Fe^{3+}	2.0×10^{-4}	Single emission	10^{-4}–10^{-3} M (R^2 = 0.978)	[51]
Eu-MOF [Eu, 2-(3′,4′-dicarboxylphenoxy)isophthalic acid, 4,4′-bis(imidazolyl) biphenyl	Fe^{3+} $Cr_2O_7^{2-}$	1.32×10^{-5} 1.01×10^{-5}	Single emission	0–10^{-5} M (R^2 = 0.9885, R^2 = 0.9927)	[52]

3.11. Mechanism Study

The mechanism of Fe^{3+} and $Cr_2O_7^{2-}$ on $Eu_{0.075}Tb_{0.925}$-MOF fluorescence sensing is examined. Figure 10a shows that the UV absorption spectrum of Fe^{3+} overlaps with the excitation spectrum of $Eu_{0.075}Tb_{0.925}$-MOF, which indicates that Fe^{3+} and $Eu_{0.075}Tb_{0.925}$-MOF are competitively adsorbed. At the same time, Figure 4 shows that Fe^{3+} is attached to the

surface of $Eu_{0.075}Tb_{0.925}$-MOF and that the interaction between Fe^{3+} and the uncoordinated O atom in the ligand is weak. $Eu_{0.075}Tb_{0.925}$-MOF reduces the energy transfer from the ligand to Tb^{3+}, and Tb^{3+} is quenched. As a result, the energy transfer from the ligand to Eu^{3+} is increased, and the characteristic red fluorescence of Eu^{3+} is displayed. Figure 10b shows that the UV absorption spectrum of $Cr_2O_7^{2-}$ overlaps with the excitation spectrum of $Eu_{0.075}Tb_{0.925}$-MOF, which indicates that $Cr_2O_7^{2-}$ and $Eu_{0.075}Tb_{0.925}$-MOF are competitively adsorbed. It will also cause the energy transfer from the ligand to Eu^{3+} to increase and show the characteristic red fluorescence of Eu^{3+}.

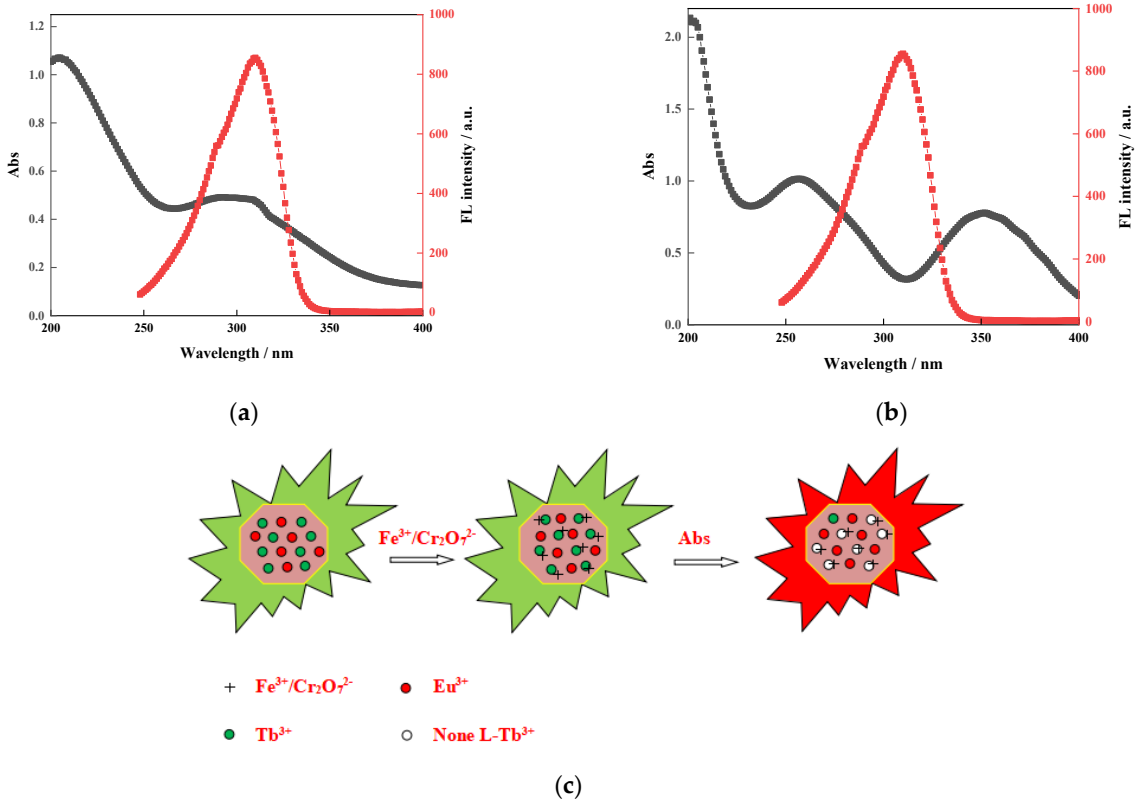

Figure 10. (**a**) Fluorescence excitation spectra of $Eu_{0.075}Tb_{0.925}$-MOF and UV-Vis absorption spectra of Fe^{3+}. (**b**) Fluorescence excitation spectra of $Eu_{0.075}Tb_{0.925}$-MOF and UV-Vis absorption spectra of $Cr_2O_7^{2-}$. (**c**) The mechanism of Fe^{3+} and $Cr_2O_7^{2-}$ on $Eu_{0.075}Tb_{0.925}$-MOF fluorescence sensing.

3.12. Application in Actual Water Sample Analysis

The ratio fluorescent probe $Eu_{0.075}Tb_{0.925}$-MOF was used for Fe^{3+} and $Cr_2O_7^{2-}$ in tap water. The results are shown in Table 3. The sample recovery rate is 101–114%, thereby showing that the established method has high accuracy and precision for the determination of Fe^{3+} and $Cr_2O_7^{2-}$ content in actual samples.

Table 3. Determination of Fe^{3+} and $Cr_2O_7^{2-}$ in real samples (n = 3).

Sample	Spiked (nM)	Found (nM)	Recovery (%)
Tap water (Fe^{3+})	20.0	22.1	110.5
	40.0	45.7	114.3
	60.0	61.6	102.7
	800	88.7	110.9
Tap water ($Cr_2O_7^{2-}$)	20.0	20.9	104.5
	40.0	41.3	103.3
	60.0	60.9	101.5
	80.0	80.8	101.0

4. Conclusions

The ratio fluorescent probe $Eu_{0.075}Tb_{0.925}$-MOF was synthesised in this experiment by using the solvothermal method and was used for Fe^{3+} and $Cr_2O_7^{2-}$ determination. Mainly on the basis of the internal filtering effect, the characteristic fluorescence emission peak intensity of Tb^{3+} decreased, and the characteristic emission peak intensity of Eu^{3+} increased on $Eu_{0.075}Tb_{0.925}$-MOF as the concentration of Fe^{3+} and $Cr_2O_7^{2-}$ increased. The ratio of the emission fluorescence intensity at the two wavelengths has a linear relationship with the target concentration, which realises the selective detection of Fe^{3+} and $Cr_2O_7^{2-}$. The linear detection range was 10–100 μM, and the LOD was 2.71×10^{-7} and 8.72×10^{-7} M, respectively. The synthesised material was used as a ratio fluorescent probe, which can effectively eliminate background fluorescence interference in the detection process and improve the detection accuracy. The trend of the fluorescence colour change of the synthesised material during the detection process indicates that the material is expected to realise naked-eye detection of Fe^{3+} and $Cr_2O_7^{2-}$.

Author Contributions: Conceptualisation, H.C.; methodology, J.Y.; investigation, J.Y. and H.C.; resources, H.C.; validation, J.Y., H.C. and S.Q.; formal analysis, J.Y. and H.C.; data curation, J.Y.; writing—original draft preparation, J.Y.; writing—review and editing, J.Y. and H.C.; supervision, H.C., S.Q., H.Q. and M.H.; project administration, H.C.; funding acquisition, H.C. All authors have read and agreed to the published version of the manuscript.

Funding: This research was funded by Research and Innovation Platform Project of Fundamental Scientific Research Business Expenses for Undergraduate Universities in Heilongjiang Province, grant number [135509304].

Acknowledgments: We are very grateful for the financial support provided by Research and Innovation Platform Project of Fundamental Scientific Research Business Expenses for Undergraduate Universities in Heilongjiang Province (135509304) for this research.

Conflicts of Interest: The authors declare no conflict of interest.

References

1. Saod, W.M.; Awad, S.S.; Mokadem, K. Assessment of some physico-chemical and microbial pollutants in the water of the Euphrates River between the cities of Hit and Fallujah in Iraq. *Desalin. Water Treat.* **2021**, *211*, 331–337. [CrossRef]
2. Salonen, J.T.; Nyyssonen, K.; Korpela, H.; Tuomilehto, J.; Seppanen, R.; Salonen, R. High stored iron levels are associated with excess risk of myocardial infarction in eastern finnish men. *Circulation* **1992**, *86*, 803–811. [CrossRef]
3. Bijeh, N.; Hejazi, K. The effect of aerobic exercise on serum ferritin levels in untrained middle-aged women. international journal of sport studies. *Int. J. Sport Stud.* **2012**, *2*, 379–384.
4. Jehn, M.L.; Guallar, E.; Clark, J.M.; Couper, D.; Duncan, B.B. A prospective study of plasma ferritin level and incident diabetes the atherosclerosis risk in communities (aric) study. *Am. J. Epidemiol.* **2007**, *165*, 1047–1054. [CrossRef]
5. Fatih, S.; Demir, D. Investigation of reduction kinetics of $Cr_2O_7^{2-}$ in $FeSO_4$ solution. *Chem. Eng. J.* **2008**, *143*, 161–166.
6. Mansi, G.; Desikan, R.; Annamalai, S.K. In situ electro-organic synthesis of hydroquinone using anisole on MWCNT/Nafion modified electrode surface and its heterogeneous electrocatalytic reduction of toxic Cr(VI) species. *RSC Adv.* **2021**, *11*, 4062–4076.
7. Costa, M. Toxicity and carcinogenicity of Cr(VI) in animal models and humans. *Crit. Rev. Toxicol.* **1997**, *27*, 431–442. [CrossRef] [PubMed]
8. Guo, X.Y.; Zhao, F.; Liu, J.J.; Liu, Z.; Wang, Y.Q. An ultrastable zinc–organic framework as a recyclable multi-responsive luminescent sensor for Cr^{3+}, Cr^{6+} and 4-nitrophenol in the aqueous phase with high selectivity and sensitivity. *J. Mater. Chem. A* **2017**, *5*, 20035–20043. [CrossRef]
9. Wang, B.G.; Lin, Y.; Tan, H.; Luo, M.; Dai, S.S.; Lu, H.S. One-pot synthesis of n-doped carbon dots by pyrolyzing the gel composed of ethanolamine and 1-carboxyethyl-3-methylimidazolium chloride and their selective fluorescence sensing for Cr^{6+} ions. *Analyst* **2018**, *143*, 1906–1915. [CrossRef]
10. Hyman, L.M.; Franz, K.J. Probing oxidative stress: Small molecule fluorescent sensors of metal ions, reactive oxygen species, and thiols. *Coord. Chem. Rev.* **2012**, *256*, 2333–2356. [CrossRef]
11. Yang, W.; Li, X.; Li, Y.; Zhu, R.; Pang, H. Applications of metal-organic-framework-derived carbon materials. *Adv. Mater.* **2019**, *31*, 1804740. [CrossRef] [PubMed]
12. Luo, T.Y.; Das, P.; White, D.L. Luminescence "turn-on" detection of gossy polusing Ln^{3+}-basedmetal-organic frameworks and Lnsalts. *J. Am. Chem. Soc.* **2020**, *142*, 2897–2904. [CrossRef]

13. Ye, J.; Bogale, R.F.; Shi, Y.; Chen, Y.; Liu, X.; Zhang, S.; Yang, Y.; Zhao, J.; Ning, G. A water-stable dual-channel luminescence sensor for UO_2^{2+} ions based on an anionic terbium(III) metal-organic framework. *Chem. A Eur. J.* **2017**, *23*, 7657–7662. [CrossRef] [PubMed]
14. Liu, W.; Wang, Y.; Bai, Z.; Li, Y.; Wang, Y.; Chen, L.; Xu, L.; Chai, Z.; Wang, S. A hydrolytically stable luminescent cationic metal-organic framework for highly sensitive and selective sensing of chromate anion in natural water systems. *ACS Appl. Mater. Interfaces* **2017**, *9*, 16448–16457. [CrossRef]
15. Wang, J.; Zhang, Q.S.; Dou, W.; Kirillov, A.M.; Liu, W.S.; Xu, C.; Xu, C.L.; Fang, R.; Yang, L.Z. Novel double layer lanthanide metal–organic networks for sensing applications. *Dalton Trans.* **2018**, *47*, 465–474. [CrossRef]
16. Liu, Q.; Tan, J.Y.; Zhang, J.Y.; Zhang, N.; Deng, W. R-substituents induced structural diversity, synergistic effect and highly selective luminescence sensing for Fe^{3+} detection by postsynthetically modified Cd-MOF. *CrystEngComm* **2020**, *22*, 3871–3883. [CrossRef]
17. Chen, J.; Chen, T.; Xiang, S.; Zhang, J.; Zhang, Z. Triazine based MOFs with abundant n sites for selective nitrobenzene detection. *Z. Anorg. Allg. Chem.* **2021**, *647*, 1301–1304. [CrossRef]
18. Li, Y.W.; Li, J.; Wan, X.Y.; Sheng, D.F.; Sun, D. Nanocage-based n-rich metal–organic framework for luminescence sensing toward Fe^{3+} and Cu^{2+} ions. *Inorg. Chem.* **2021**, *60*, 671–681. [CrossRef]
19. Ye, Y.; Guo, W.; Wang, L.; Li, Z.; Song, Z.; Chen, J.; Zhang, Z.; Xiang, S.; Chen, B. Straightforward loading of imidazole molecules into metal-organic framework for high proton conduction. *J. Am. Chem. Soc.* **2017**, *139*, 15604–15607. [CrossRef] [PubMed]
20. Karmakar, A.; Samanta, P.; Desai, A.V.; Ghosh, S.K. Guest-responsive metal organic frameworks as scaffolds for sand sensing Applications. *Acc. Chem. Res.* **2017**, *50*, 2457–2469. [CrossRef]
21. Li, X.; Xie, Y.J.; Song, B. A stimuli-responsive smart lanthanide nanocomposite for multidimensional optical recording and encryption. *Angew. Chem. Int. Ed.* **2017**, *56*, 2689–2693. [CrossRef] [PubMed]
22. Yuan, Y.Y.; Yang, S.L.; Zhang, C.; Wang, Q.L. A new europium metal–organic framework with both high proton conductivity and highly sensitive detection of ascorbic acid. *CrystEngComm* **2018**, *20*, 6989–6994. [CrossRef]
23. Yin, H.Q.; Wang, X.Y.; Yin, X.B. Rotation restricted emission and antenna effect in single metal-organic frameworks. *J. Am. Chem. Soc.* **2019**, *141*, 15166–15173. [CrossRef]
24. Li, H.; Cao, X.; Fei, X.; Zhang, S.; Xian, Y. Nanoscaled luminescent terbium metal–organic frameworks for measuring and scavenging reactive oxygen species in living cells. *J. Mater. Chem. B* **2019**, *7*, 3027–3033. [CrossRef]
25. Liu, S.; Liu, M.; Guo, M.; Wang, Z.; Tian, Z. Development of Eu-based metal-organic frameworks (MOFs) for luminescence sensing and entrapping of arsenate ion. *J. Lumin.* **2021**, *236*, 118102. [CrossRef]
26. Abdelhamid, H.N. and Sharmoukh, W. Intrinsic catalase-mimicking mofzyme for sensitive detection of hydrogen peroxide and ferric ions. *Microchem. J.* **2021**, *163*, 105873. [CrossRef]
27. Gai, Y.; Guo, Q.; Zhao, X.; Yan, C.; Xiong, K.C. Extremely stable europium-organic framework for luminescent sensing of $Cr_2O_7^{2-}$ and Fe^{3+} in aqueous systems. *Dalton Trans.* **2018**, *47*, 12051–12055. [CrossRef]
28. Cui, Y.J.; Xu, H.; Yue, Y.F. A luminescent mixed-lanthanide metal-organic framework thermometer. *J. Am. Chem. Soc.* **2012**, *134*, 3979–3982. [CrossRef] [PubMed]
29. Rao, X.T.; Song, T.; Gao, J.K.; Cui, Y.; Qian, G. A highly sensitive mixed lanthanide metal-organic framework self-calibrated luminescent thermometer. *J. Am. Chem. Soc.* **2013**, *135*, 15559–15564. [CrossRef]
30. Zhang, S.Y.; Wei, S.; Cheng, P.; Zaworotko, M.J. A mixed-crystal lanthanide zeolite-like metal–organic framework as a fluorescent indicator for lysophosphatidic acid, a cancer biomarker. *J. Am. Chem. Soc.* **2015**, *137*, 12203–12206. [CrossRef]
31. Yan, B.; Xu, X.Y. Fabrication and application of a ratiometric and colorimetric fluorescent probe for Hg^{2+} based on dual-emissive metal–organic framework hybrids with carbon dots and Eu^{3+}. *J. Mater. Chem. C* **2016**, *4*, 1543–1549.
32. Wu, J.X.; Yan, B. A dual-emission probe to detect moisture and water in organic solvents based on green-Tb^{3+} post-coordinated metal–organic frameworks with red carbon dots. *Dalton Trans.* **2017**, *46*, 7098–7105. [CrossRef]
33. Xin, F.; Rui, L.; Jian, S.; Hui, L.; Xin, L. A dual-emission nano-rod MOF equipped with carbon dots for visual detection of doxycycline and sensitive sensing of MnO_4. *RSC Adv.* **2018**, *8*, 4766–4772.
34. Jintana, O.; Boonmak, J.; Promarak, V. Sonochemical synthesis of carbon dots/lanthanoid MOFs hybrids for white light-emitting diodes with high color rendering. *ACS Appl. Mater. Interfaces* **2019**, *11*, 44421–44429.
35. Gao, J.P.; Yao, R.X.; Chen, X.H.; Li, H.H.; Zhang, X.M. Blue luminescent N,S-doped carbon dots encapsulated in red emissive Eu-MOF to form dually emissive composite for reversible anti-counterfeit ink. *Dalton Trans.* **2020**, *50*, 1690–1696. [CrossRef]
36. Silva, M.A.; Campos, N.R.; Ferreira, L.A.; Flores, L.S.; Júnior, J.A.; Santos, G.L.; Corrêa, C.C.; Santos, T.C.; Ronconi, C.M.; Colaço, M.V.; et al. A new photoluminescent terbium(III) coordination network constructed from 1,2,4,5-benzenetetracarboxylic acid: Synthesis, structural characterization and application as a potential marker for gunshot residues. *Inorg. Chim. Acta* **2019**, *495*, 118967. [CrossRef]
37. Hu, X.F.; Wang, Z.Y.; Su, Y.M.; Chen, P.C.; Chen, J.W.; Zhang, C.K.; Wang, C. Nanoscale metal−organic frameworks and metal−organic layers with two-photon-excited fluorescence. *Inorg. Chem.* **2020**, *59*, 4181–4185. [CrossRef]
38. Hao, J.N.; Yan, B. A dual-emitting 4d–4f nanocrystalline metal–organic framework as a self-calibrating luminescent sensor for indoor formaldehyde pollution. *Nanoscale* **2016**, *8*, 12047–12053. [CrossRef]
39. Zhou, L.M.; Gao, L.J.; Fang, S.M.; Sun, G.H.; Hu, M.; Guo, L.Q.; Han, C.; Zhang, L.C. Preparation and characterization of novel transparent Eu(AA)3-polyurethane acrylate copolymeric materials. *J. Appl. Polym. Sci.* **2012**, *125*, 690–696. [CrossRef]

40. Yang, C.; Liu, S.; Xu, J.; Li, Y.; Shang, M.; Lei, L.; Wang, G.; He, J.; Wang, X.; Lu, M. Efficient red emission from poly(vinyl butyral) films doped with a novel europium complex based terpyridyl as ancillary ligand: Synthesis, structural elucidation by Sparkle/RM1 calculation, and photophysical properties. *Polym. Chem.* **2016**, *7*, 1147–1157. [CrossRef]
41. Wang, Y.M.; Tian, X.T.; Zhang, H.; Yang, Z.R.; Yin, X.B. Anticounterfeiting quick response code with emission color of invisible metal-organic frameworks as encoding information. *Acs Appl. Mater. Interfaces* **2018**, *10*, 22445–22452. [CrossRef] [PubMed]
42. Wu, S.; Lin, Y.; Liu, J.; Shi, W.; Yang, G.; Cheng, P. Rapid detection of the biomarkers for carcinoid tumors by a water stable luminescent lanthanide metal-organic framework sensor. *Adv. Funct. Mater.* **2018**, *28*, 1707169. [CrossRef]
43. Su, Y.; Zhang, D.; Jia, P.; Gao, W.; Li, Y.; He, J.; Wang, C.; Zheng, X.; Yang, Q.; Yang, C. Bonded-luminescent foam based on europium complexes as a reversible copper (II) ions sensor in pure water. *Eur. Polym. J.* **2019**, *112*, 461–465. [CrossRef]
44. Su, Y.; Zhang, D.; Jia, P.; Gao, W.; Li, Y.; Bai, Z.; Liu, X.; Deng, Q.; Xu, J.; Yang, C. Highly selective and sensitive long fluorescence lifetime polyurethane foam sensor based on Tb-complex as chromophore for the detection of $H_2PO_4^-$ in water. *Spectrochim. Acta Part A Mol. Biomol. Spectrosc.* **2019**, *217*, 86–92. [CrossRef] [PubMed]
45. Fedorova, K.A.; Sokolovskii, G.S.; Khomylev, M.; Livshits, D.A.; Rafailov, E.U. Efficient yellow-green light generation at 561nm by frequency-doubling of a QD-FBG laser diode in a PPLN waveguide. *Opt. Lett.* **2014**, *39*, 6672–6674. [CrossRef] [PubMed]
46. Gao, W.; Feng, L.; Zhang, B.Y.; Zhang, X.M.; Liu, J.P.; Gao, E.Q. 2D carboxylate-bridged LnIII coordination polymers: Displaying slow magnetic relaxation and luminescence properties in the detection of Fe^{3+}, $Cr_2O_7^{2-}$ and nitrobenzene. *Dalton Trans.* **2017**, *46*, 13878–13887. [CrossRef]
47. Ma, J.J.; Liu, W.S. Effective luminescence sensing of Fe^{3+}, $Cr_2O_7^{2-}$, MnO_4^- and 4-nitrophenol by lanthanide metal–organic frameworks with a new topology type. *Dalton Trans.* **2019**, *48*, 12287–12295. [CrossRef] [PubMed]
48. Li, B.; Dong, J.P.; Zhou, Z.; Wang, R.; Zang, S.Q. Robust lanthanide metal–organic frameworks with "all-in-one" multifunction: Efficient gas adsorption and separation, tunable light emission and luminescent sensing. *J. Mater. Chem. C* **2021**, *9*, 3429–3439. [CrossRef]
49. Xu, H.; Hu, H.C.; Cao, C.S.; Zhao, B. Lanthanide organic framework as a regenerable luminescent probe for Fe^{3+}. *Inorg. Chem.* **2015**, *54*, 4585–4587. [CrossRef]
50. Kang, Y.; Zheng, X.J.; Jin, L.P. A microscale multi-functional metal-organic framework as a fluorescence chemosensor for Fe^{3+}, Al^{3+} and 2-hydroxy-1-naphthaldehyde. *J. Colloid Interface* **2016**, *6*, 1–6. [CrossRef]
51. Gu, J.Z.; Cai, Y.; Liu, Y.; Liang, X.X.; Kirillov, A.M. New lanthanide 2d coordination polymers constructed from a flexible ether-bridged tricarboxylate block: Synthesis, structures and luminescence sensing. *Inorg. Chim. Acta* **2018**, *1*, 98–104. [CrossRef]
52. Du, Y.; Yang, H.Y.; Liu, R.J.; Shao, C.Y.; Yang, L.R. A multi-responsive chemosensor for highly sensitive and selective detection of Fe^{3+}, Cu^{2+}, $Cr_2O_7^{2-}$ and nitrobenzene based on a luminescent lanthanide metal–organic framework. *Dalton Trans.* **2020**, *49*, 13003–13016. [CrossRef] [PubMed]